RSC Advances

PAPER

View Article Online
View Journal | View Issue



Cite this: *RSC Adv.*, 2017, **7**, 47602

# Hierarchical flower-like $NiCo_2O_4$@$TiO_2$ hetero-nanosheets as anodes for lithium ion batteries

Wei Chen,[abc] Luya Wei,[a] Zhiya Lin,[a] Qian Liu,[a] Yue Chen,[a] Yingbin Lin *[abc] and Zhigao Huang [abc]

Received 15th August 2017
Accepted 5th October 2017

DOI: 10.1039/c7ra09024b

rsc.li/rsc-advances

Flower-like $NiCo_2O_4$ consisting of nanosheets are synthesized by hydrothermal technique and subsequently surface-modified with a $TiO_2$ ultrathin layer by a hydrolysis process at low temperature. It is found that $NiCo_2O_4$@$TiO_2$ exhibits superior electrochemical performances over $NiCo_2O_4$ in terms of rate capability and cyclability. After 60 cycles at 100 mA $g^{-1}$, $NiCo_2O_4$@$TiO_2$ showed 78% capacity retention compared with 57% for bare $NiCo_2O_4$. Analysis from the electrochemical measurements indicates that the improved electrochemical performances of $NiCo_2O_4$@$TiO_2$ might be attributed to a higher lithium diffusion rate, smaller charge-transfer resistance and more structural stability. Kelvin probe force microscopy measurements reveal that $NiCo_2O_4$@$TiO_2$ has a lower work function than those of the pristine one, which help to facilitate electron transfer in composites. In addition, the electric field between $NiCo_2O_4$ and $TiO_2$ resulting from the difference in work functions is also expected to enhance the electrochemical performances.



## 1. Introduction

Owing to their advantages on lifespan and energy density, rechargeable lithium-ion batteries have attracted increasing interest due to their wide application in energy storage systems (ESSs) and electric vehicles (EV/HEV/PHEV).[1–5] The increasing demands for high-energy or high-power batteries are driving the research interest in electrode materials with a large specific energy.[6–8] Unfortunately, graphite or carbon-based materials with low theoretical specific capacity (*ca.* 372 mA h $g^{-1}$) are not highly desirable for the high energy-density batteries.[9,10] In contrast, binary metal oxides, such as $ZnFe_2O_4$, $NiFe_2O_4$, $ZnMn_2O_4$ and $NiCo_2O_4$, seem to be a more promising alternative because of their high theoretical capacity and high redox activity.[11–14] Among the numerous investigated binary metal oxides, spinel nickel cobaltite ($NiCo_2O_4$) has been regarded as a promising electrode composite due to the high specific capacity (890 mA h $g^{-1}$), environmental friendliness and low cost.[15,16] However, $NiCo_2O_4$ also suffers from sluggish reaction kinetics and drastic volume change during lithium insertion/extraction processes, resulting in the structure deterioration (pulverization or aggregation) and consequent severe decay in capacity.[17,18] To address above significant drawbacks, lots of effective strategies have been implemented and surface-modification has been proved to be an effective way to improve electrochemical performances, which not only suppresses the formation of excessive amounts of SEI but also stabilizes structure of the active materials.[19] Kou *et al.*[19] reported that $Al_2O_3$-coated $NiCo_2O_4$ exhibits improved cyclability with a reversible capacity of 395 mA h $g^{-1}$ after 50 cycles. Titanium oxide ($TiO_2$) has been investigated extensively as an anode material, whose volume expansion is less than 4% during the lithium insertion processes.[20,21] The low volume expansion would be desirable for adhesion of the coating to the matrix materials, resulting in the enhanced structural stability and a excellent cycle life. On the other hand, $TiO_2$-coating layer acting as an interfacial barrier can also significantly enhance cyclic performances by suppressing the exothermic reaction between the active material and the electrolyte.

In view of all the above, we employ hydrolysis technique to coat $TiO_2$ on flower-like $NiCo_2O_4$ consisting of nanosheets at low temperature, and the effect of $TiO_2$-coating on the kinetics of $Li^+$ insertion/extraction is systematically investigated. It is found that the high capacity of $NiCo_2O_4$ and the excellent stability of $TiO_2$ as well as the hierarchical structure make the designed composite demonstrate improved rate capability and cycling stability.

## 2. Experimental

### 2.1 Preparation and characterization of anode materials

Flower-like $NiCo_2O_4$ consisting of nanosheets are prepared by hydrothermal technique. All chemicals are purchased from

[a]*College of Physics and Energy, Fujian Normal University, Fujian Provincial Key Laboratory of Quantum Manipulation and New Energy Materials, Fuzhou, 350117, China. E-mail: yblin@fjnu.edu.cn; Fax: +86-591-2286-8132; Tel: +86-591-2286-8132*

[b]*Fujian Provincial Engineering Technology Research Center of Solar Energy Conversion and Energy Storage, Fuzhou, 350117, China*

[c]*Fujian Provincial Collaborative Innovation Center for Optoelectronic Semiconductors and Efficient Devices, Xiamen, 361005, China*

Aladin and used without further purification. In a typical synthesis, 6 mmol of $Ni(NO_3)_2 \cdot 6H_2O$ and 12 mmol of $Co(NO_3)_2 \cdot 6H_2O$ are thoroughly dissolved in 30 ml of deionized water and 30 ml of absolute ethanol, followed by stirring until a light pink solution is formed. Then, 0.1 g of polyvinyl pyrrolidone (PVP) is added to the above aqueous solution under continuous stirring. After vigorous stirring for another 60 min, the resulted mixture is transferred into a 100 ml Teflon-lined autoclave, sealed and maintained at 180 °C for 36 h. After being cooled to room temperature, the precipitates are collected through centrifugation, washed several times with de-ionized water and ethanol, dried at 100 °C overnight under vacuum. The obtained precursors (Ni–Co–O) are calcinated at 450 °C for 5 h in air to get flower-like $NiCo_2O_4$ powders. $NiCo_2O_4$@$TiO_2$ composites are synthesized by a hydrolysis process at low temperature using tetrabutyl titanate ($Ti(OC_4H_9)_4$) and Ni–Co–O powders as precursors. 0.23 g of the as-prepared Ni–Co–O precursors are dispersed in 20 ml of absolute ethanol and 1 ml of deionized water under vigorous stirring at 4 °C. Then, 10 ml $10^{-3}$ M $Ti(OC_4H_9)_4$ ethanol solution is added dropwise into above solution. After stirring at 4 °C for another 24 h, the resulting precipitates are isolated by centrifugation, dried at 60 °C for 12 h and subsequently sintered at 450 °C for 5 h to obtain flower-like $NiCo_2O_4$ surface-modified with $TiO_2$. The schematic illustration of the synthesis process for the $NiCo_2O_4$ and $NiCo_2O_4$@$TiO_2$ characterized anode materials is shown in Fig. 1.

The crystalline structure of the as-synthesized powders is characterized by X-ray diffraction (XRD, Rigaku MiniFlex II) using $CuK_\alpha$ radiation ($\lambda = 0.15405$ nm). Thermo-gravimetric analysis (TGA) analysis are carried out using thermogravimetric analysis (TGA, Netzsch STA449F3) from 30 to 600 °C at a heating rate of 5 °C $min^{-1}$ under an air atmosphere. Scanning electron microscope (SEM) images are obtained on a Hitachi SU8010 field-emission scanning electron microscope equipped with an energy-dispersive spectroscopy (EDS). The $TiO_2$ content in the composite is determined by inductively coupled plasma OES spectrometer (ICP). Raman scattering is carried out on a Horiba/Jobin Yvon Raman instrument using a 532 nm emission line. Nitrogen sorption isotherms are measured at 77 K using a Micromeritics Tristar 3020 analyzer. Specific surface areas of the as-prepared powders are calculated according to the Brunauer–Emmett–Teller (BET) method. The pore size distribution is determinated according to the theory of Barrett, Joyner and Halenda (BJH).

The surface potentials of $NiCo_2O_4$ and $NiCo_2O_4$@$TiO_2$ are measured by Kelvin probe atomic force microscopy (KPAFM) (Bruker dimension ICON, Germany).

### 2.2 Cell fabrication and characterization

The electrochemical performances of the as-fabricated samples are evaluated with CR2025-type coin cell and assembled in an argon-filled glove box ($O_2$, $H_2O$ < 1 ppm). The working electrodes are prepared by coating anode slurries which are made up of 70 wt% active material ($NiCo_2O_4$ or $NiCo_2O_4$@$TiO_2$) with 10 wt% polyvinylidene fluoride (PVDF) and 20 wt% super-P in *N*-methyl-2-pyrrolidone. The anode slurry is cast onto a copper current collector and dried in vacuum at 110 °C for 12 h to remove the residual solvent. A lithium foil is used as the reference and counter electrodes, Cellgard 2300 microporous polyethylene membrane as separator. The electrolyte consists of 1 M

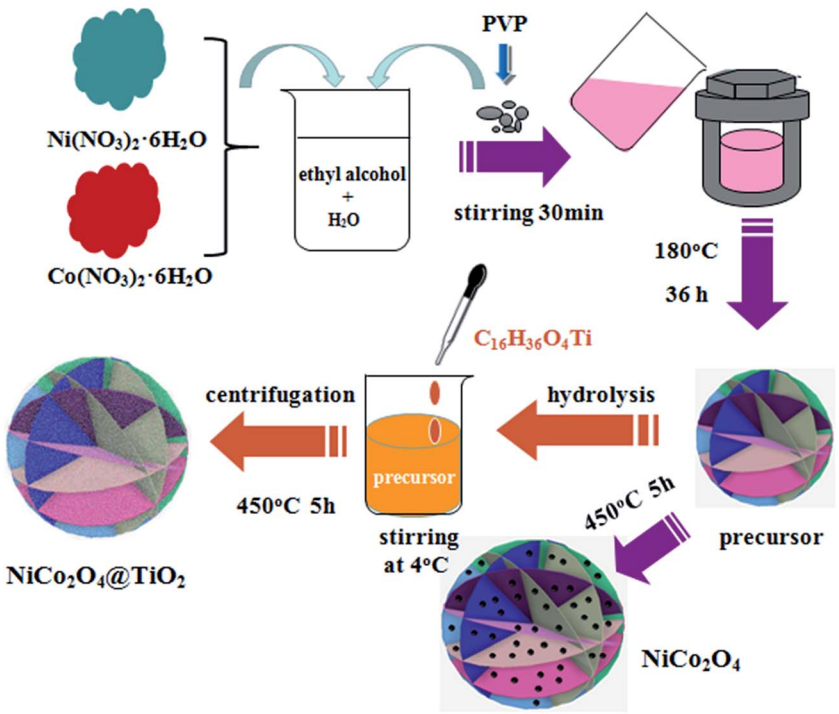


Fig. 1 Schematic illustration of the preparation process for $NiCo_2O_4$ and $NiCo_2O_4$@$TiO_2$ powders.

$LiPF_6$ in a mixture of ethylene carbonate (EC) and dimethyl carbonate (DMC) (1 : 1 in volume). The cells are galvanostatically charged and discharged on a multichannel battery testing system (Land CT2001A, Wuhan, China) in the voltage range of 0.01–2.5 V. The cyclic voltammetry (CV) measurements are carried out using an Arbin instruments BT-2000 battery testing station, and the electrochemical impedance spectra of the electrodes are determined by an electrochemical workstation (Zahner-Zennium) in the frequency range of 100 kHz to 10 mHz with an amplitude of 5 mV.

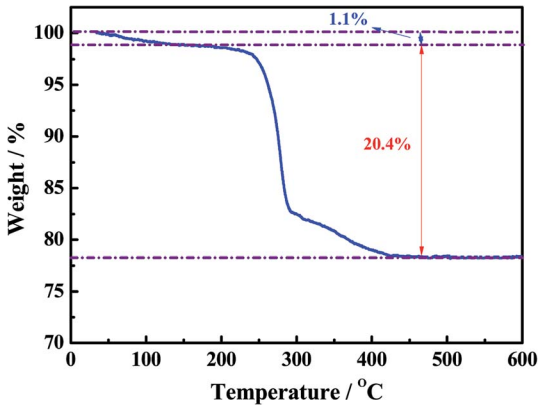


Fig. 2 TGA curves of the Ni–Co precursor in air atmosphere.

## 3. Results and discussion

### 3.1 Material characterization

Fig. 2 shows the thermogravimetric (TGA) curve of the as-synthesized Ni–Co–O precursor, measured from 30 to 800 °C at a heating rate of 3 °C $min^{-1}$ in air atmosphere. The initial 1.1% weight loss at the low temperature (30–250 °C) would result from the loss of the evaporation of moisture and the decomposition of crystal water in the precursor. The following 20.4% weight loss with a big step occurs between 250 and 450 °C, which might be attributed to the conversion of anhydrous precursors to spinel cubic crystals. Therefore, we reasonably chose 450 °C as calcination temperature in our experiment.

The morphology and microstructure of the as-prepared $NiCo_2O_4$ and $NiCo_2O_4$@$TiO_2$ powders are characterized by scanning electron microscopy as shown in Fig. 1. It is clear that $NiCo_2O_4$ powders are all rose flower-like morphology (Fig. 3(a)), which is composed of thin transparent nanosheets with a thickness of ~20 nm. Fig. 3(b) reveals that the nanosheets of $NiCo_2O_4$ contains many micro-pores, which is mainly attributed to the organics loss accompanying removal of PVP and gases during the calcination process.[22,23] Such hierarchical structure would be

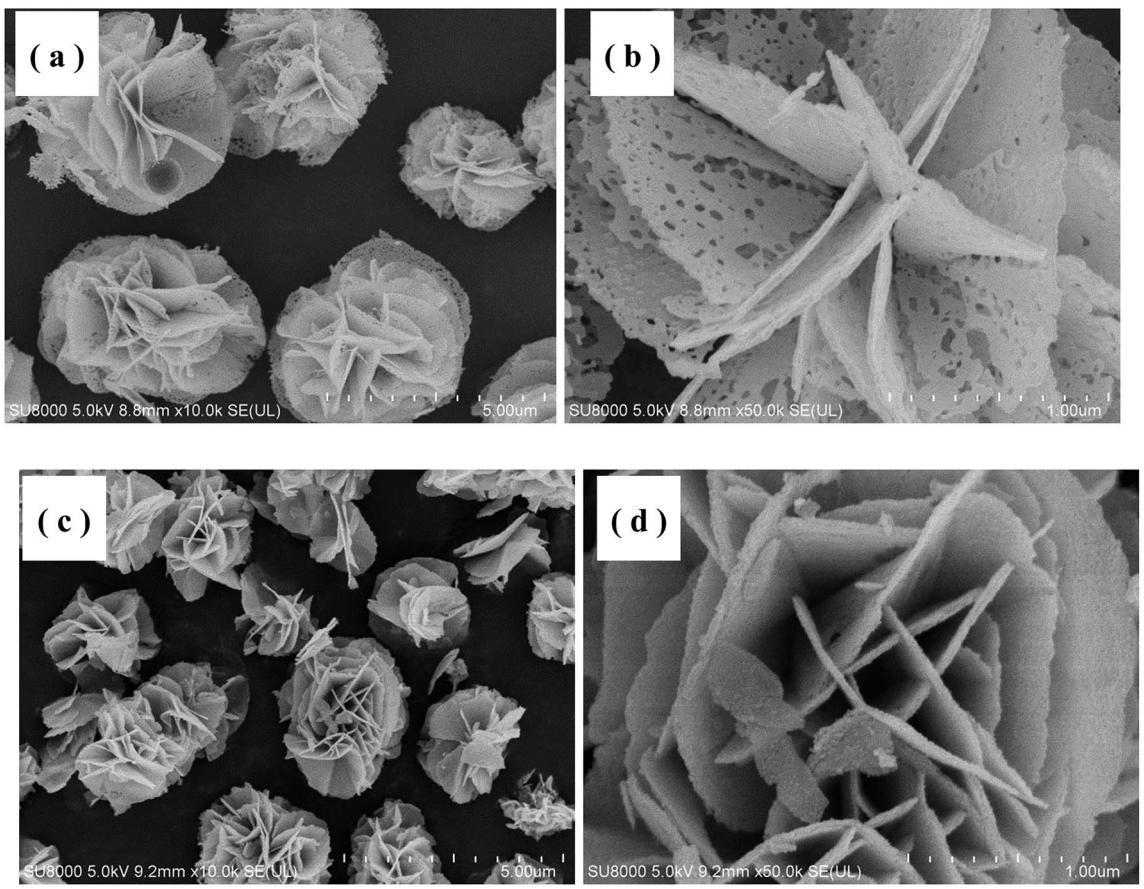


Fig. 3 SEM images of the as-prepared $NiCo_2O_4$ and $NiCo_2O_4$@$TiO_2$ powders.

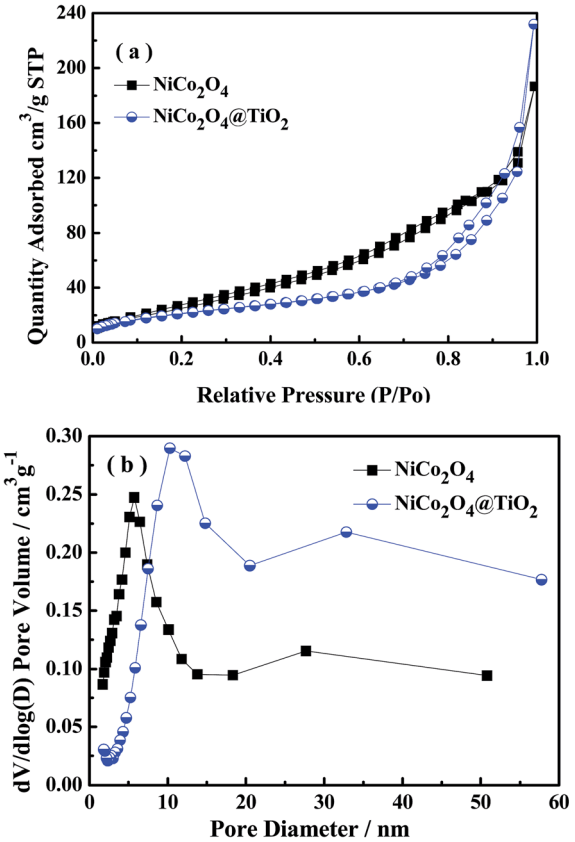


Fig. 4 (a) Nitrogen sorption isotherms and (b) pore diameter distribution of $NiCo_2O_4$ and $NiCo_2O_4$@$TiO_2$ powders.

highly desirable for rapid Li-ion diffusion and electron transfer. Porosity structure of the $NiCo_2O_4$ nanosheet may be benefit for lithium-ion transportation from the electrolyte into the active sites with less resistance, and buffer efficiently large volume expansion during the Li-ion insertion/extraction processes.[24] With $TiO_2$-coating, $NiCo_2O_4$@$TiO_2$ powders also maintain the nanosheet-built flower-like nanostructure as same to the bare one, shown in Fig. 3(c). In contrast, the nanosheets of $NiCo_2O_4$@$TiO_2$ have a smooth and integrated surface morphology and the micro-pores on the "petals" disappears, indicating $TiO_2$ layer is uniformly coated on the nanosheet surface.

Fig. 4(a) presents nitrogen adsorption–desorption isotherms of $NiCo_2O_4$ and $NiCo_2O_4$@$TiO_2$ powders, indicating a typical hysteresis mesoporous system.[12,25] According to Brunauer–Emmett–Teller (BET) equation, the specific surface areas of $NiCo_2O_4$ and $NiCo_2O_4$@$TiO_2$ are calculated to be 98.78 and 78.09 $m^2\ g^{-1}$, respectively. Fig. 4(b) shows the corresponding pore-size distribution based on Barrett–Joyner–Halenda (BJH) method, indicating that $NiCo_2O_4$@$TiO_2$ have larger average pore size (10.3 nm) that (5.6 nm) of $NiCo_2O_4$. An increase in average pore size and reduction in surface area could be reasonably explained by the disappearance of micro-pores (5.6 nm) because of $TiO_2$-coating. The obtained results are consistent with the analysis from SEM images. The distribution of corresponding elements of $NiCo_2O_4$@$TiO_2$ is investigated by EDS. Element mapping images for Ni, Co and Ti in $NiCo_2O_4$@$TiO_2$ powders (Fig. 5) reveal that the corresponding elements uniformly distribute on the surface of the $NiCo_2O_4$@$TiO_2$ particles.

Fig. 6(a) shows the XRD patterns of $NiCo_2O_4$ and $NiCo_2O_4$@$TiO_2$ powders. All of the diffraction peaks are characteristic

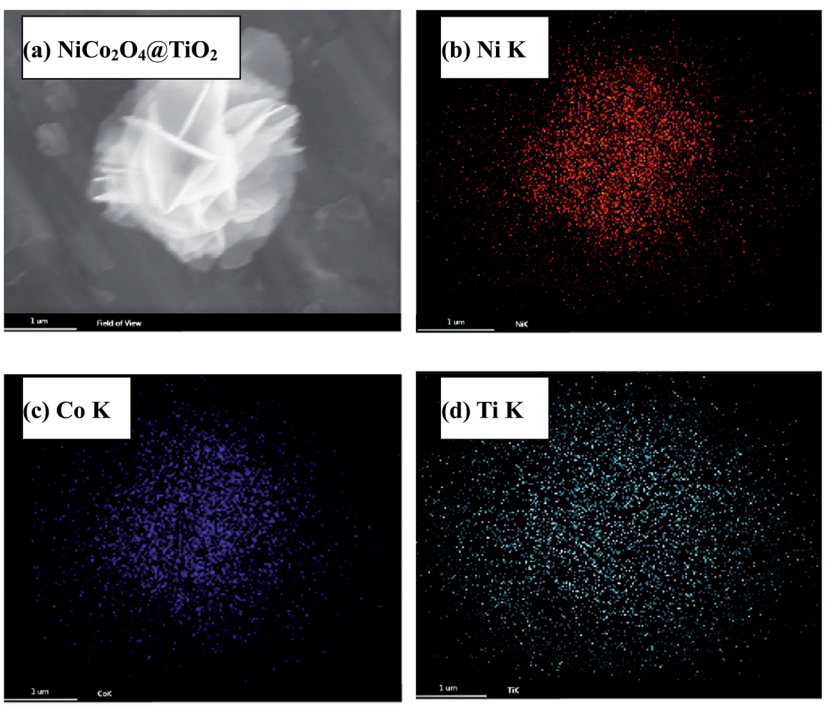


Fig. 5 Element mapping images of $NiCo_2O_4$@$TiO_2$ powders.

of a spinel $NiCo_2O_4$ structure with space group *Fd3m* (JCPDS card no. 73–1702).[22,26] It is found that no visible differences in XRD patterns between two composites, which is attributed to the low content of $TiO_2$ phase. Fig. 6(b) presents Raman spectra of the as-prepared $NiCo_2O_4$@$TiO_2$ samples. Five obvious peaks at 212, 313, 366, 536 and 671 $cm^{-1}$ are found in the Raman spectrum of $NiCo_2O_4$@$TiO_2$ composites, which can be assigned to the vibrational modes of spinel $NiCo_2O_4$.[27,28] The peak at around 149 $cm^{-1}$ is related to the $E_g$ vibration modes of the $TiO_2$ anatase structure.[29] The $TiO_2$ content in $NiCo_2O_4$@$TiO_2$ composite is further determined to be *ca.* 3.53 wt% by inductively coupled plasma OES spectrometer (ICP).

The elemental composition and the oxidation state of the $NiCo_2O_4$@$TiO_2$ powder is further characterized by X-ray photoelectron spectroscopy (XPS) measurements and the corresponding results are present in Fig. 7(a–e). The survey spectrum (Fig. 7(a)) reveals the presence of Ni, Co, Ti and O as well as C elements without any other impurities. By using a Gaussian fitting method, the Ni 2p core-level spectrum (Fig. 7(b)) has two spin–orbit doublets and two shake-up satellites, which are in good agreement with the characteristic of $Ni^{2+}$ and $Ni^{3+}$.[30] Similarly, two spin–orbit doublets and shake-up satellites can also be observed in the Co 2p spectrum, corresponding to the characteristic of $Co^{2+}$ and $Co^{3+}$.[30] The peaks located at 458.7 and 464.4 eV are attributed to the Ti $2p_{3/2}$ and Ti $2p_{1/2}$ spin–orbit doublets, indicating the predominant state of the Ti element in composite is $Ti^{4+}$.[31] The O 1s spectra can be divided into two main oxygen peaks at 529.6 and 531 eV. The peak located at 529.6 eV is typical characteristic of metal–oxygen bonds.[32] The XPS results are in good agreement with the analysis from XRD and ED measurements.

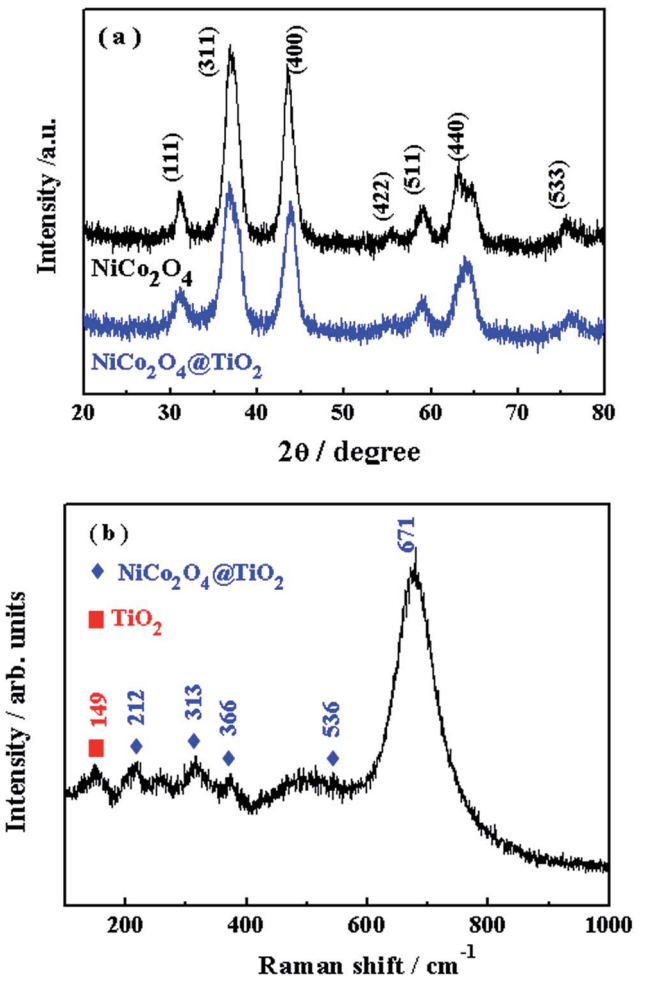


Fig. 6 (a) XRD patterns of $NiCo_2O_4$ and $NiCo_2O_4$@$TiO_2$ powders; (b) Raman spectra of the as-prepared $NiCo_2O_4$@$TiO_2$ powders.

Fig. 8(a) shows the rate capabilities of $NiCo_2O_4$ and $NiCo_2O_4$@$TiO_2$ electrodes at various current density, measured from 100 to 2000 mA $g^{-1}$ in rising order and subsequently followed by returning 1000, 500 and 200 mA $g^{-1}$. In comparison, $NiCo_2O_4$@$TiO_2$ composite exhibits better rate performance than that of the bare one, especially at a higher rate. When the current density increases to 100, 200, 500, 1000 and 2000 mA $g^{-1}$, the $NiCo_2O_4$@$TiO_2$ electrode shows reversible discharge capacities of 988, 930, 840, 750 and 624 mA h $g^{-1}$, respectively. Even at a high current density of 2000 mA $g^{-1}$, the discharge capacity still retains 63.2%. When the current density returns back to 1000, 500 and 200 mA $g^{-1}$, the $NiCo_2O_4$@$TiO_2$ electrode still recovers 735, 837 and 1004 mA h $g^{-1}$, indicating excellent structure stability of the nano-composite. In contrast, the $NiCo_2O_4$ electrode delivers a lower discharge capacity at current density. The discharge capacities of the $NiCo_2O_4$ electrode are measured to be 983, 878, 778, 683 and 562 mA $g^{-1}$ at the same respective current density. It has been reported that small anatase $TiO_2$ particles would be turning from an insulator into an electronic conductor during the $Li^+$ insertion possess.[33,34] Therefore, $TiO_2$-coating on $NiCo_2O_4$ nanosheets is beneficial for both structural stability as well as the rate capability.

Fig. 8(b) presents the cycling performance of $NiCo_2O_4$ and $NiCo_2O_4$@$TiO_2$ electrodes at a current density of 100 mA $g^{-1}$. In comparison with $NiCo_2O_4$, the capacity loss is significantly suppressed after coating with $TiO_2$. The initial discharge capacity at 100 mA $g^{-1}$ of $NiCo_2O_4$ is 1424 mA h $g^{-1}$ and found to decrease to 815 mA h $g^{-1}$ after 60 cycles (*i.e.*, only 57% of its initial discharge capacity). The discharge capacity of the $NiCo_2O_4$@$TiO_2$ is found to decay gradually with continuous cycling, retaining 78% of its maximum discharge capacity after 60 cycles. In addition, the coulombic efficiency of $NiCo_2O_4$ is relatively low and unstable, which might result from the SEI formation repeatedly on $NiCo_2O_4$ nanosheet during the charge/discharge processes.[19] Similar results are reported in Lotfabad's work.[33] Here, we have made a comparison of the electrochemical performances between our $NiCo_2O_4$@$TiO_2$ and other $NiCo_2O_4$ with different morphologies previously reported, as summarized in Table 1. It is found that $NiCo_2O_4$@$TiO_2$ nanocomposites exhibit superior cycling stability, indicating its potential application in high-energy lithium-ion batteries.

Fig. 9(a and b) shows cyclic voltammetry profiles of $NiCo_2O_4$ and $NiCo_2O_4$@$TiO_2$ electrode for the first six cycles at a scan rate of 0.1 mV $s^{-1}$ and from 0.01 to 2.5 V. Two peaks are observed at around 0.6 and 0.9 V in the initial cathodic sweep for both samples, which are assigned to the formation of the solid electrolyte interface layer and the reaction of $Co^{3+}$ and $Ni^{2+}$ to $Co^0$ and $Ni^0$, respectively.[41] Two oxidation peaks at around 1.4

 

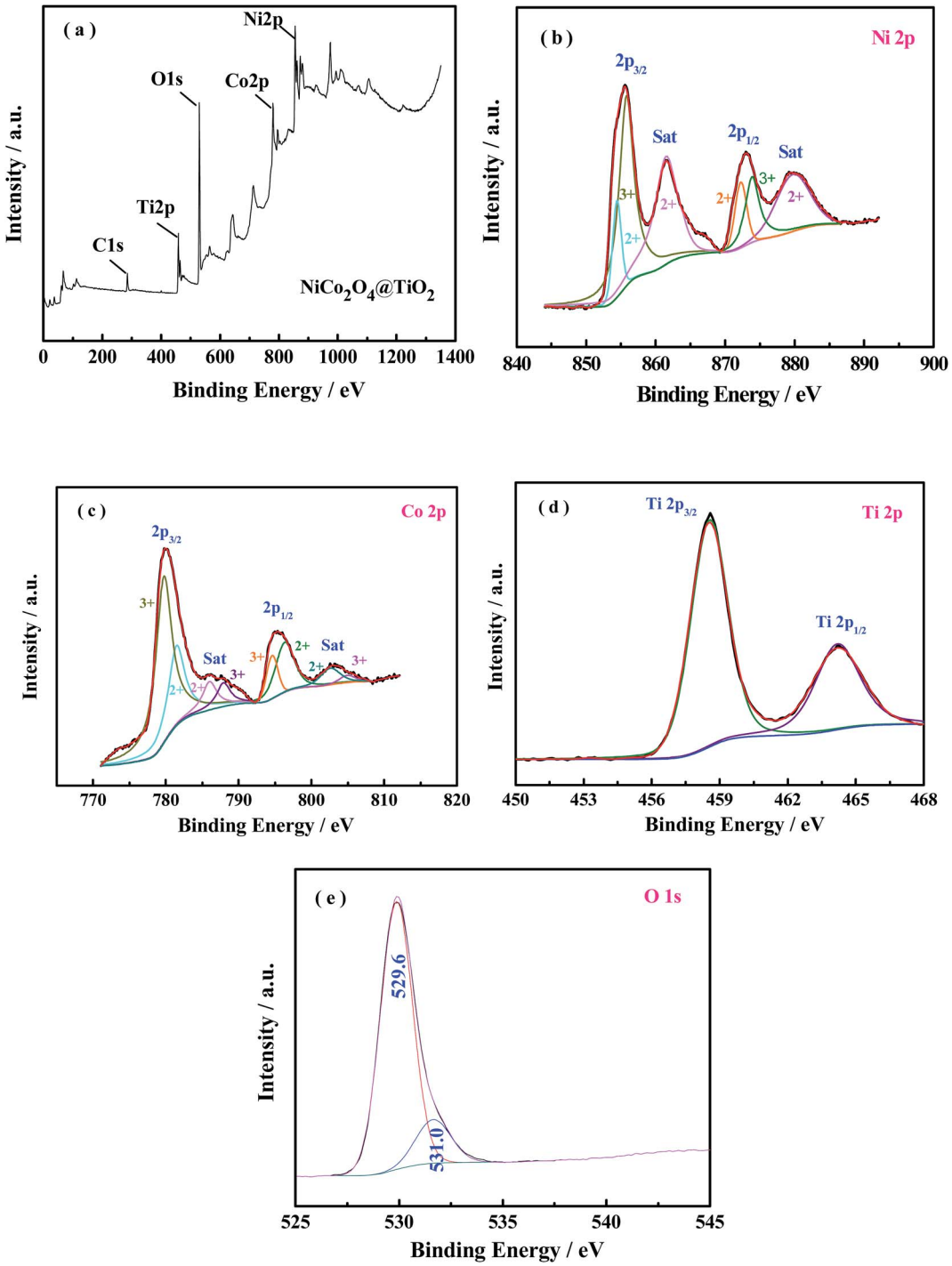


Fig. 7 XPS spectra of (a) survey spectrum, (b) Ni 2p, (c) Co 2p, (d) Ti 2p and (e) O 1s for the $NiCo_2O_4$@$TiO_2$ product.

and 2.2 V are also observed in the initial anodic sweep, which are attributed to the oxidation of $Co^0$ and $Ni^0$ to $Co^{3+}$ and $Ni^{2+}$, respectively.[42] According to the previous reports,[43] the redox reactions can be expressed as follows:

$$NiCo_2O_4 + 8Li^+ + 8e^- \rightarrow Ni + 2Co + 4Li_2O \quad (1)$$

$$Ni + Li_2O \leftrightarrow NiO + 2Li^+ + 2e^- \quad (2)$$

$$Co + Li_2O \leftrightarrow CoO + 2Li^+ + 2e^- \quad (3)$$

$$CoO + 1/3Li_2O \leftrightarrow 1/3Co_3O_4 + 2/3Li^+ + 2/3e^- \quad (4)$$

In comparison with $NiCo_2O_4$, the CV curves from 2nd to 6th cycles for $NiCo_2O_4$@$TiO_2$ exhibit a better overlapping degree, indicating a better reversibility of the electrochemical reactions.

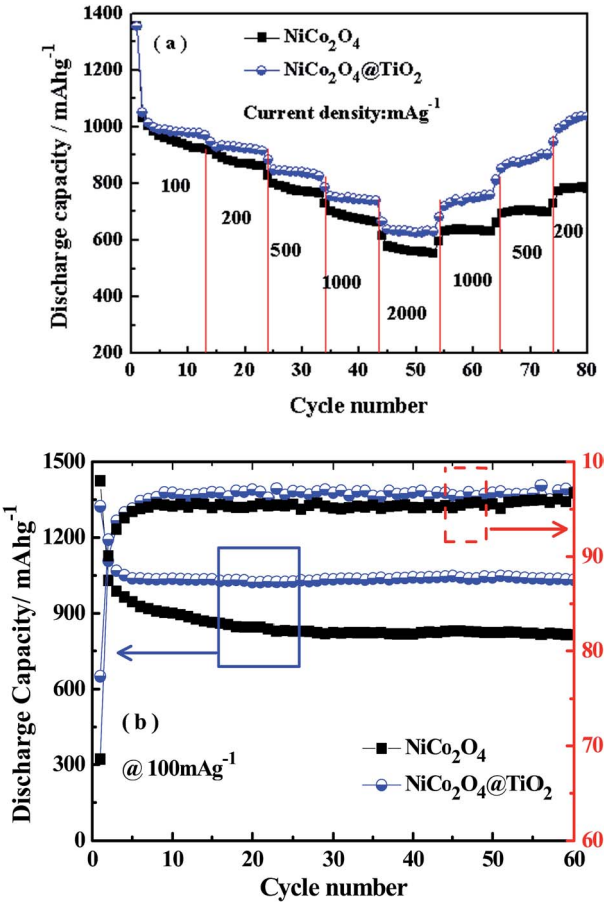


Fig. 8 (a) Rate capability and (b) cyclic performances of $NiCo_2O_4$ and $NiCo_2O_4$@$TiO_2$ electrodes.

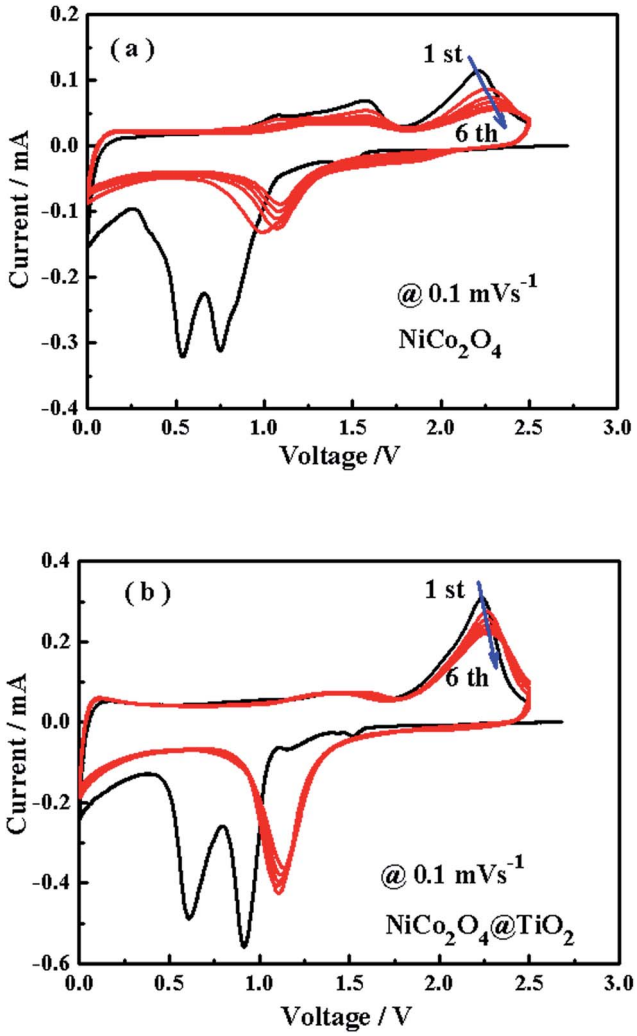


Fig. 9 Cyclic voltammetry profiles of $NiCo_2O_4$ and $NiCo_2O_4$@$TiO_2$ electrodes.

Table 1 Comparison of the electrochemical performances of the $NiCo_2O_4$@$TiO_2$ electrode in this work with other similar materials reported previously

| Materials | Current density (mA g$^{-1}$) | Capacity (mA h g$^{-1}$) | Ref. |
|---|---|---|---|
| Plum-like $NiCo_2O_4$ | 0.1 | 801 after 50 cycles | 22 |
| $NiCo_2O_4$/3DGN | 0.5 | 790 after 50 cycles | 35 |
| $NiCo_2O_4$/Ni | 0.1 | 413 after 50 cycles | 36 |
| $NiCo_2O_4$@$SnO_2$@C-HSs | 0.1 | 720 after 100 cycles | 37 |
| $NiCo_2O_4$@G | 0.3 | 806 after 55 cycles | 38 |
| $NiCo_2O_4$ nanosheets | 0.1 | 767 after 50 cycles | 17 |
| $NiCo_2O_4$@RGO | 0.1 | 816 after 70 cycles | 39 |
| $NiCo_2O_4$@$NiCo_2O_4$ NCAs | 0.12 | 830 after 100 cycles | 40 |
| $NiCo_2O_4$@$TiO_2$ | 0.1 | 1033 after 60 cycles | This work |

To further investigate the potential mechanism behind the improved performances with surface-modified of $TiO_2$ layer, the cells after cycling are disassembled, washed, dried in vacuum and characterized by SEM. Fig. 10 presents the morphologies of $NiCo_2O_4$ and $NiCo_2O_4$@$TiO_2$ powders characterized by SEM after 10 and 30 cycles, respectively. It is obvious that $NiCo_2O_4$ powders has serious structure-deterioration (pulverization or aggregation) and losses its flower-like structure with increasing cycles due to the repeated volume change between metals and metal oxides. The aggregation of the active materials tends to reduce the effective contact areas between active materials and the electrolyte. In contrast, $NiCo_2O_4$@$TiO_2$ powders can remain in the flower-like structure well, which further confirms that $TiO_2$-layer would stabilize structure of the active materials and consequently offer more active sites during the lithium-ion insertion/extraction process. Combined with the analysis of the SEM images after cycling, it is expected that stable hierarchical nanostructures are desirable for the improved electrochemical performances.

Electrochemical impedance spectra are carried out to get insight into the improved rate and cyclic performances of $NiCo_2O_4$@$TiO_2$. Fig. 11(a) presents the typical EIS of $NiCo_2O_4$ and $NiCo_2O_4$@$TiO_2$ electrode in the fully discharged state. Both EIS profiles consist of two depressed semicircles in the medium-to-high frequency range and a straight line in the low-frequency region. According to the equivalent circuit in the inset of Fig. 11(a), the charge-transfer resistance ($R_{ct}$) are

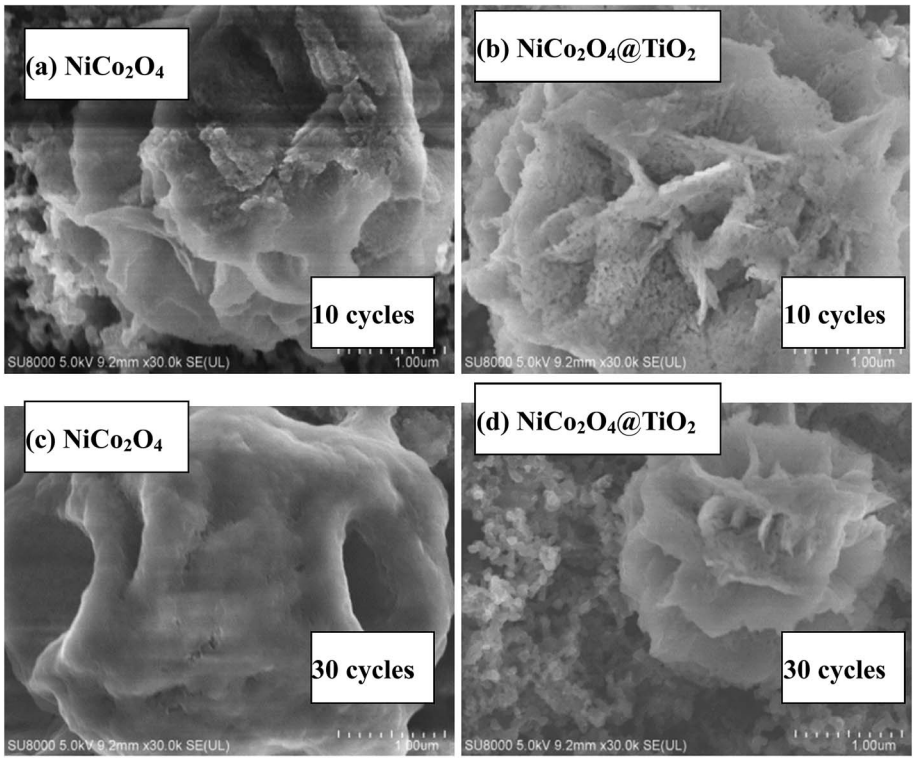


Fig. 10 SEM images of the $NiCo_2O_4$ and $NiCo_2O_4$@$TiO_2$ powders after 10 and 30 cycles, respectively.

calculated as 36.6 Ω for $NiCo_2O_4$ and 20.4 Ω for $NiCo_2O_4$@$TiO_2$, respectively. The decrease in $R_{ct}$ for $NiCo_2O_4$@$TiO_2$ would derive from the more stable structure by $TiO_2$-coating with continuous cycling.[44] The $TiO_2$-coating layer is expected to efficiently prevent the pulverization of $NiCo_2O_4$ during the $Li^+$ intercalation/extraction process and mediate the increase in charge transfer resistance of the composites, which facilitates Li-ions transfer at the interface between the active material and electrolyte. As a result, the electrochemical performances are improved.

The diffusion coefficients ($D_{Li}$) of the Li-ion kinetic of the cells can be also calculated according to the EIS profiles in the low frequency.

$$\sigma = \frac{RT}{n^2F^2A\sqrt{2}}\left(\frac{1}{C_{Li}D_{Li}{}^{1/2}}\right) \quad (5)$$

$$Z_{re} = R + \sigma\omega^{-1/2} \quad (6)$$

$R$, $T$ and $F$ are the mass gas constant, absolute temperature and Faraday's constant; $A$, $n$ and $C_{Li}$ are the surface area of the electrode, the number of electrons per molecule during oxidation and the molar volume of active material; $\sigma$, $Z_{re}$ and $\omega$ are the Warburg factor, the real part of the impedance and the frequency. Based on the slope coefficient of $Z_{re}$ to $\omega^{-1/2}$ (see Fig. 11(b)), the corresponding lithium diffusion coefficients $D_{Li}$ of $NiCo_2O_4$ and $NiCo_2O_4$@$TiO_2$ powders are calculated as $2.57 \times 10^{-12}$ $cm^2$ $s^{-1}$ and $8.18 \times 10^{-12}$ $cm^2$ $s^{-1}$ respectively, suggesting the rapid diffusion of lithium-ions of $NiCo_2O_4$@$TiO_2$ electrode.

To evaluate the effect of $TiO_2$-coating on the Li-ion diffusion during the charge/discharge process, the impedance spectra under different discharge states for $NiCo_2O_4$ and $NiCo_2O_4$@$TiO_2$ electrodes are continuously measured, shown in Fig. 12(a and b). According to eqn (5) and (6), the corresponding $Li^+$-ion diffusion coefficients of $NiCo_2O_4$ and $NiCo_2O_4$@$TiO_2$ electrodes are calculated. Fig. 12(c) presents lithium-ion diffusion behaviors during the lithium-ion insertion process. Both electrodes demonstrate similar lithium-ion diffusion behavior. On the whole, $NiCo_2O_4$@$TiO_2$ electrode exhibits larger $Li^+$ diffusion coefficients than those of the bare one, indicating that $TiO_2$-coating does readily facilitate the $Li^+$ diffusion in composites. It is worth noting that $NiCo_2O_4$@$TiO_2$ electrode has much larger diffusion coefficients of lithium-ions in the voltage range from 1.0 to 0.01 V, which might be attributed to the lithium ion insertion in $TiO_2$. It is expected that lithium-inserted $Li_xTiO_2$ anatase would turn from an insulator into an electronic conductor during the $Li^+$ insertion possess, resulting in enhanced electron-transfer in composites.[33] As a result, $TiO_2$ coating on $NiCo_2O_4$ is potentially beneficial for the improved rate capability as well as the structural integrity of the composite.

Kelvin probe atomic force microscopy is used to study the influence of $TiO_2$-coating on the Li-ion kinetic behavior in composites. Fig. 13(a and b) shows the surface potential maps over a scan area of 200 nm × 200 nm of $NiCo_2O_4$ and $NiCo_2O_4$@$TiO_2$ powders before cycling. Fig. 13(c) presents the surface potential image of Au foil acting as reference sample. According to our prior work,[45] the work functions of $NiCo_2O_4$ and $NiCo_2O_4$@$TiO_2$ powders are calculated based on the surface potential

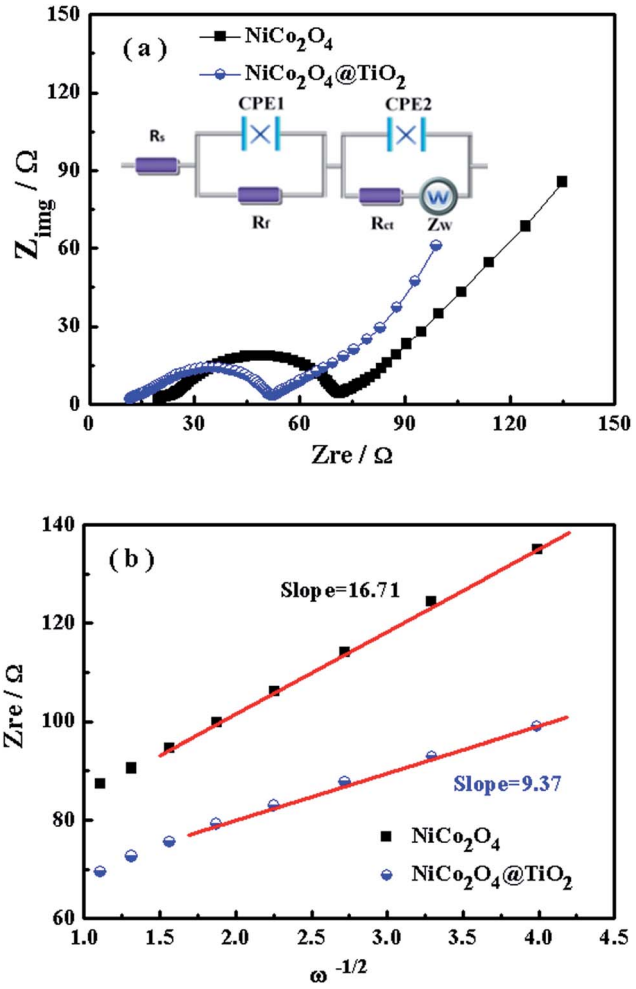


Fig. 11 (a) Typical EIS of $NiCo_2O_4$ and $NiCo_2O_4$@$TiO_2$ electrode in the fully discharged state and the equivalent circuit for EIS fitting; (b) real parts of the complex impedance $Z_{re}$ *vs.* $\omega^{-1/2}$ for $NiCo_2O_4$ and $NiCo_2O_4$@$TiO_2$ electrodes.

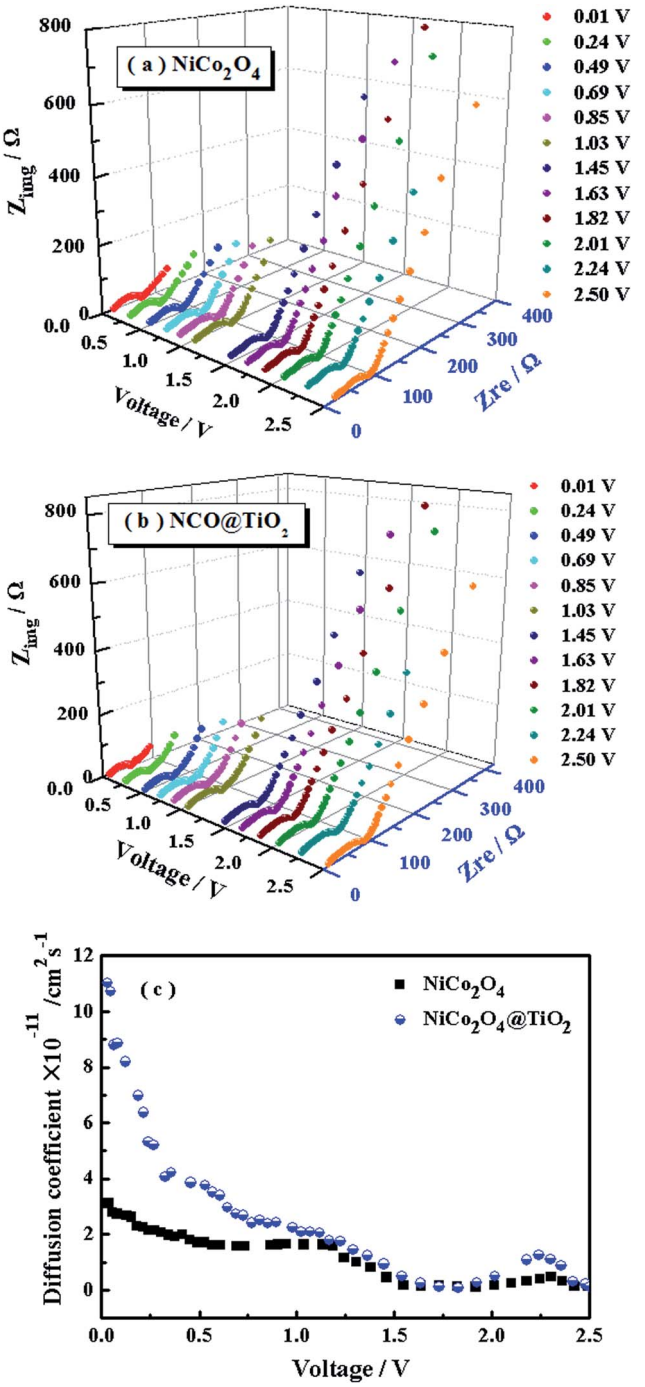


Fig. 12 (a, b) The impedance spectra and (c) corresponding Li-ion of diffusion coefficients of $NiCo_2O_4$ and $NiCo_2O_4$@$TiO_2$ electrodes under different discharge states.

profiles and the corresponding results are shown in Fig. 13(d). Here, the work functions of the SFM-tip ($\phi_{tip}$) is calibrated by Au foil, whose work function ($\phi_{Au}$) is 5.31 eV. It is found that $NiCo_2O_4$@$TiO_2$ has a smaller work function (~5.41 eV) than that (~5.51 eV) of the $NiCo_2O_4$. The measured work function of $NiCo_2O_4$ is close to the reported value (5.53 eV).[46,47] The larger work function suggests the more energy required for electrons to escape from the composites. As a result, the electrochemical performances of the composites are enhanced with surface-modified with $TiO_2$-coating. These obtained results are consist with the analysis of EIS measurements.

The reduced work function of $NiCo_2O_4$@$TiO_2$ could be explained phenomenologically based on the energy-band model. As shown in Fig. 14(a), electrons transfer occurs from $TiO_2$ to $NiCo_2O_4$ until the Fermi levels are aligned due to the smaller work function (~4.5 eV) of anatase $TiO_2$.[48] As a result, the $TiO_2$ is positively charged and the $NiCo_2O_4$ is negatively charged near its surface due to electrostatic induction because of electrostatic induction. Meanwhile, a corresponding electric field ($E$) is built up between them, shown in Fig. 14(b). Such electric field could facilitate Li-ion diffusion from positively-charged $TiO_2$ to negatively-charged $NiCo_2O_4$, and electron transfer from $NiCo_2O_4$ to $TiO_2$ across heterojunction interfaces. With the help of the electric field, more electrons in $NiCo_2O_4$ matrix would transfer through $TiO_2$ rather than $NiCo_2O_4$/$NiCo_2O_4$ interface during the lithium insertion process. Moreover, $TiO_2$ coated on $NiCo_2O_4$ could effectively suppress the pulverization of $NiCo_2O_4$ matrix due to the volume change in

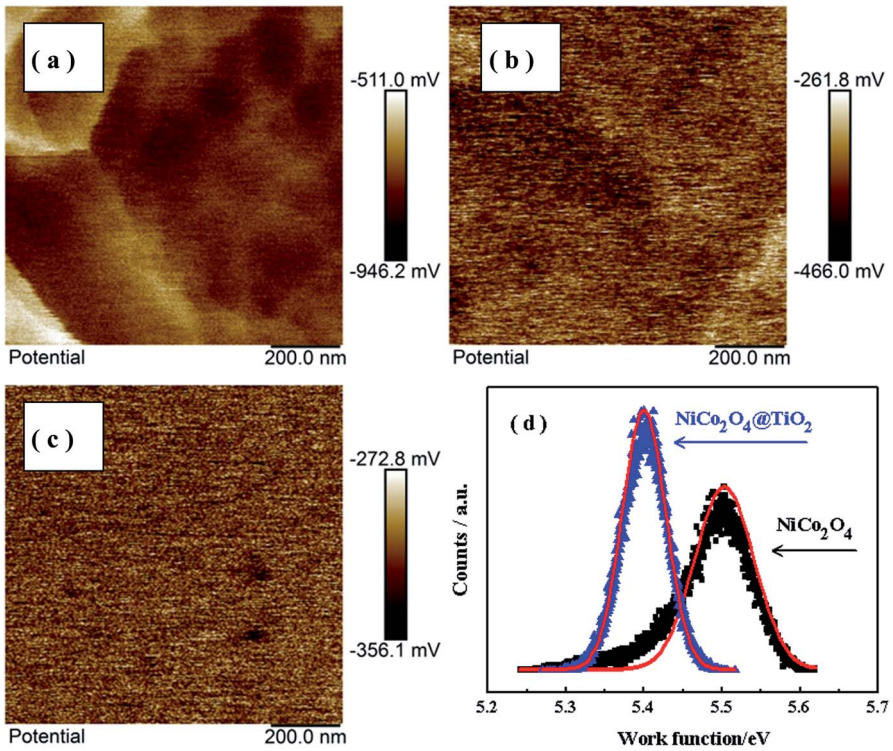


Fig. 13 (a, b) Surface potential maps over a scan area of 200 nm × 200 nm of $NiCo_2O_4$ and $NiCo_2O_4$@$TiO_2$ powders before cycling; (c) surface potential image of Au foil acting as reference sample; (d) work functions of $NiCo_2O_4$ and $NiCo_2O_4$@$TiO_2$ electrodes.

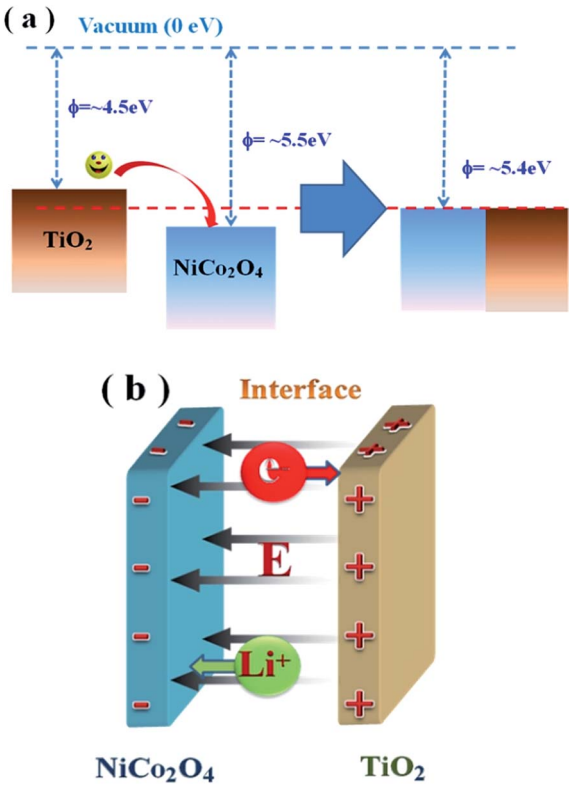


Fig. 14 (a) The energy-level model for explaining the improved electron transfer in $NiCo_2O_4$@$TiO_2$ electrodes; (b) a built electric field (*E*) between $NiCo_2O_4$ and $TiO_2$.

the charge/discharge process. As a result, the electrochemical performances are enhanced.

## Conflicts of interest

There are no conflicts to declare.

## Acknowledgements

This work is supported by a grant from Key Project of Department of Science & Technology of Fujian Province (No. 2014H0020), Program for New Century Excellent Talents in University of Fujian Province (No. JA14069) and Project A of Education Bureau of Fujian Province (No. JA12067).

## References

1 M. Armand and J.-M. Tarascon, Building better batteries, *Nature*, 2008, **451**, 652–657.
2 J. B. Goodenough, Electrochemical energy storage in a sustainable modern society, *Energy Environ. Sci.*, 2014, **7**, 14–18.
3 R. A. Huggins, Review—a new class of high rate, long cycle life, aqueous electrolyte battery electrodes, *J. Electrochem. Soc.*, 2017, **164**, A5031–A5036.
4 J. Lu, Z. H. Chen, Z. F. Ma, F. Pan, A. L. Curtiss and K. Amine, The role of nanotechnology in the development of battery materials for electric vehicles, *Nat. Nanotechnol.*, 2016, **11**, 1031–1038.

5 G. E. Blomgren, The development and future of lithium ion batteries, *J. Electrochem. Soc.*, 2017, **164**, A5019–A5025.
6 Z. Y. Wang, L. Zhou and X. W. Lou, Metal oxide hollow nanostructures for lithium-ion batteries, *Adv. Mater.*, 2012, **24**, 1903–1911.
7 M. V. Reddy, G. V. S. Rao and B. V. R. Chowdari, Metal oxides and oxysalts as anode materials for Li ion batteries, *Chem. Rev.*, 2013, **113**, 5364–5457.
8 M. Freire, N. V. Kosova, C. Jordy, D. Chateigner, O. I. Lebedev, A. Maignan and V. Pralong, A new active Li-Mn-O compound for high energy density Li-ion batteries, *Nat. Mater.*, 2016, **15**, 173–177.
9 H. Buqa, D. Goers, M. Holzapfel, M. E. Spahr and P. Novák, High rate capability of graphite negative electrodes for lithium-ion batteries, *J. Electrochem. Soc.*, 2005, **152**, A474–A481.
10 J. F. Li, S. L. Xiong, Y. R. Liu, Z. C. Ju and Y. T. Qian, High electrochemical performance of monodisperse $NiCo_2O_4$ mesoporous microspheres as an anode material for Li-ion batteries, *ACS Appl. Mater. Interfaces*, 2013, **5**, 981–988.
11 B. B. Jiang, C. P. Han, B. Li, Y. J. He and Z. Q. Lin, In-situ crafting of $ZnFe_2O_4$ nanoparticles impregnated within continuous carbon network as advanced anode materials, *ACS Nano*, 2016, **10**, 2728–2735.
12 R. C. Jin, H. Jiang, Y. X. Sun, Y. Q. Ma, H. H. Li and G. Chen, Fabrication of $NiFe_2O_4$/C hollow spheres constructed by mesoporous nanospheres for high-performance lithium-ion batteries, *Chem. Eng. J.*, 2016, **303**, 501–510.
13 X. Q. Chen, Y. M. Zhang, H. B. Lin, P. Xia, X. Cai, X. G. Li, X. P. Li and W. S. Li, Porous $ZnMn_2O_4$ nanospheres: facile synthesis through microemulsion method and excellent performance as anode of lithium ion battery, *J. Power Sources*, 2016, **312**, 137–145.
14 G. Zhou, C. Wu, Y. H. Wei, C. C. Li, Q. W. Lian, C. Cui, W. F. Wei and L. B. Chen, Tufted $NiCo_2O_4$ nanoneedles grown on carbon nanofibers with advanced electrochemical property for lithium ion batteries, *Electrochim. Acta*, 2016, **222**, 1878–1886.
15 C. Zhang and J. S. Yu, Morphology-tuned synthesis of $NiCo_2O_4$-Coated 3D graphene architectures used as binder-free electrodes for lithium-ion batteries, *Chem.–Eur. J.*, 2016, **22**, 4422–4430.
16 Y. Lei, J. Li, Y. Wang, L. Gu, Y. Chang, H. Yuan and D. Xiao, Rapid microwave-assisted green synthesis of 3D hierarchical flower-shaped $NiCo_2O_4$ microsphere for high-performance supercapacitor, *ACS Appl. Mater. Interfaces*, 2014, **6**, 1773–1780.
17 A. K. Mondal, D. W. Su, S. Q. Chen, K. Kretschmer, X. Q. Xie, H. J. Ahn and G. X. Wang, A microwave synthesis of mesoporous $NiCo_2O_4$ nanosheets as electrode materials for lithium-ion batteries and supercapacitors, *ChemPhysChem*, 2015, **16**, 169–175.
18 L. L. Li, S. J. Peng, Y. L. Cheah, P. F. Teh, J. Wang, G. Wee, Y. Ko, C. L. Wong and M. Srinivasan, Electrospun porous $NiCo_2O_4$ nanotubes as advanced electrodes for electrochemical capacitors, *Chem.–Eur. J.*, 2013, **19**, 5892–5898.
19 H. R. Kou, X. F. Li, H. Shan, L. L. Fan, B. Yan and D. J. Li, An optimized $Al_2O_3$ layer for enhancing the anode performance of $NiCo_2O_4$ nanosheets for sodium-ion batteries, *J. Mater. Chem. A*, 2017, **5**, 17881–17888.
20 Z. H. Chen, I. Belharouak, Y. K. Sun and K. Amine, Titanium-based anode materials for safe lithium-ion batteries, *Adv. Funct. Mater.*, 2013, **23**, 959–969.
21 J. H. Lee, M. H. Hon, Y. W. Chung and I. C. Leu, The effect of $TiO_2$ coating on the electrochemical performance of ZnO nanorod as the anode material for lithium-ion battery, *Appl. Phys. A*, 2011, **102**, 545–550.
22 T. Li, X. Li, Z. Wang, H. Guo and Y. Li, A novel $NiCo_2O_4$ anode morphology for lithium-ion batteries, *J. Mater. Chem. A*, 2015, **3**, 11970–11975.
23 J. Xu, D. W. Su, W. Z. Bao, Y. F. Zhao, X. Q. Xie and G. X. Wang, Rose flower-like $NiCo_2O_4$ with hierarchically porous structures for highly reversible lithium storage, *J. Alloys Compd.*, 2016, **684**, 691–698.
24 F. C. Zheng, D. Q. Zhu and Q. W. Chen, Facile fabrication of porous $Ni_xCo_{3-x}O_4$nanosheets with enhanced electrochemical performance as anode materials for li-ion batteries, *ACS Appl. Mater. Interfaces*, 2014, **6**, 9256–9264.
25 Y. D. Mo, Q. Ru, X. Songa, L. Y. Guo, J. F. Chen, X. H. Hou and S. J. Hu, The sucrose-assisted $NiCo_2O_4$@C composites with enhanced lithium-storage properties, *Carbon*, 2016, **109**, 616–623.
26 A. K. Mondal, D. W. Su, S. Q. Chen, X. Q. Xie and G. X. Wang, Highly porous NiCo2O4 nanoflakes and nanobelts as anode materials for lithium-ion batteries with excellent rate capability, *ACS Appl. Mater. Interfaces*, 2014, **6**, 14827–14835.
27 H. Zheng, S. Xu, L. Li, C. Feng and S. Q. Wang, Synthesis of $NiCo_2O_4$ microellipsoids as anode material for lithium-ion batteries, *J. Electron. Mater.*, 2016, **45**, 4966–4972.
28 L. B. Ma, X. P. Shen, Z. Y. Ji, X. Q. Cai, G. X. Zhu and K. M. Chen, Porous $NiCo_2O_4$ nanosheets/reduced graphene oxide composite: facile synthesis and excellent capacitive performance for supercapacitors, *J. Colloid Interface Sci.*, 2015, **440**, 211–218.
29 Y. Zhang, W. Wu, K. Zhang, C. H. Liu, A. F. Yu, M. Z. Peng and J. Y. Zhai, Raman study of 2D anatase $TiO_2$ nanosheets, *Phys. Chem. Chem. Phys.*, 2016, **18**, 32178–32184.
30 R. X. Ge, M. Ma, X. Ren, F. L. Qu, Z. A. Liu, G. Du, A. M. Asiri, L. Chen, B. Zheng and X. Sun, A $NiCo_2O_4$@Ni–Co–Ci core–shell nanowire array as an efficient electrocatalyst for water oxidation at near-neutral pH, *Chem. Commun.*, 2017, **53**, 7812–7815.
31 M. C. Biesinger, L. W. Lau, A. R. Gerson and R. S. C. Smart, Resolving surface chemical states in XPS analysis of first row transition metals oxides and hydroxides: Sc, Ti, V, Cu and Zn, *Appl. Surf. Sci.*, 2010, **257**, 887–898.
32 Y. D. Mo, Q. Ru, X. Song, S. J. Hu, L. Y. Guo and X. Q. Chen, 3-dimensional porous $NiCo_2O_4$ nanocomposite as a high-rate capacity anode for lithium-ion batteries, *Electrochim. Acta*, 2015, **176**, 575–585.
33 E. M. Lotfabad, P. Kalisvaart, K. Cui, A. Kohandehghan, M. Kupsta, B. Olsena and D. Mitlin, ALD $TiO_2$ coated silicon nanowires for lithium ion battery anodes with

enhanced cycling stability and coulombic efficiency, *Phys. Chem. Chem. Phys.*, 2013, **15**, 13646–13657.

34 W. J. H. Borghols, D. Lutzenkirchen-Hecht, U. Haake, E. R. H. van Eck, F. M. Mulder and M. Wagemaker, The electronic structure and ionic diffusion of nanoscale $LiTiO_2$ anatase, *Phys. Chem. Chem. Phys.*, 2009, **11**, 5742–5748.

35 S. N. Liu, J. Wu, J. Zhou, G. Z. Fang and S. Q. Liang, Mesoporous $NiCo_2O_4$ nanoneedles grown on three dimensional graphene networks as binder-free electrode for high-performance lithium-ion batteries and supercapacitors, *Electrochim. Acta*, 2015, **176**, 1–9.

36 G. H. Chen, J. Yang, J. J Tang and X. Y. Zhou, Hierarchical $NiCo_2O_4$ nanowire arrays on Ni foam as an anode for lithium-ion batteries, *RSC Adv.*, 2015, **5**, 23067–23072.

37 G. X. Gao, H. B. Wu, S. J. Ding and X. W. Lou, Preparation of carbon-coated $NiCo_2O_4$@$SnO_2$ hetero-nanostructures and their reversible lithium storage properties, *Small*, 2015, **11**, 432–436.

38 Y. J. Chen, J. Zhu, B. H. Qu, B. A. Lun and Z. Xu, Graphene improving lithium-ion battery performance by construction of $NiCo_2O_4$/graphene hybrid nanosheet arrays, *Nano Energy*, 2014, **3**, 88–94.

39 Y. J. Chen, M. Zhuo, J. W. Deng, Z. Xu, Q. H. Li and T. H. Wang, Graphene improving lithium-ion battery performance by construction of $NiCo_2O_4$/graphene hybrid nanosheet arrays, *J. Mater. Chem. A*, 2014, **2**, 4449–4456.

40 J. B. Cheng, Y. Lu, K. W. Qiu, H. L. Yan, J. Y. Xu, L. Han, X. M. Liu, J. S. Luo, J. K. Kim and Y. S. Luo, Hierarchical core/shell $NiCo_2O_4$@$NiCo_2O_4$ nanocactus arrays with dual-functionalities for high performance supercapacitors and Li-ion batteries, *Sci. Rep.*, 2015, **5**, 12099.

41 Y. Chen, J. Zhu, B. Qu, B. Lu and Z. Xu, Graphene improving lithium-ion battery performance by construction of $NiCo_2O_4$/graphene hybrid nanosheet arrays, *Nano Energy*, 2014, **3**, 88–94.

42 C. F. Zhang and J. S. Yu, Morphology-tuned synthesis of $NiCo_2O_4$-coated 3D graphene architectures used as binder-free electrodes for lithium-ion batteries, *Chem.–Eur. J.*, 2016, **22**, 4422–4430.

43 L. L. Li, Y. Cheah, Y. W. Ko, P. Teh, G. Wee, C. L. Wong, S. J. Peng and M. Srinivasan, The facile synthesis of hierarchical porous flower-like $NiCo_2O_4$ with superior lithium storage properties, *J. Mater. Chem. A*, 2013, **1**, 10935–10941.

44 W. Shi, H. T. Zhao and B. G. Lu, Core–shell $ZnCo_2O_4$@$TiO_2$ nanowall arrays as anodes for lithium ion batteries, *Nanotechnology*, 2017, **28**, 165403.

45 L. C. Chen, Y. M. Yang, Z. S. Wang, J. Y. Zhang, Q. L. Su, Y. Chen, Y. B. Lin and Z. G. Huang, Enhanced electrochemical performances and thermal stability of $LiNi_{1/3}Co_{1/3}Mn_{1/3}O_2$ by surface modification with $YF_3$, *J. Alloys Compd.*, 2017, **711**, 462–472.

46 K. K. Naik, R. T Khare, R. V Gelamo, M. A More, R. Thapa, D. J. Late and C. S. Rout, Enhanced electron field emission from $NiCo_2O_4$nanosheet arrays, *Mater. Res. Express*, 2015, **2**, 095011.

47 C. Zhang, X. P. Geng, S. L. Tang, M. S. Deng and Y. W. Du, $NiCo_2O_4$@rGO hybrid nanostructures on Ni foam as high-performance supercapacitor electrodes, *J. Mater. Chem. A*, 2017, **5**, 5912–5919.

48 L. X. Zheng, S. C. Han, H. Liu, P. P. Yu and X. S. Fang, Hierarchical $MoS_2$ nanosheet@$TiO_2$ nanotube array composites with enhanced photocatalytic and photocurrent performances, *Small*, 2016, **12**, 1527–1536.